

# Microhole-Arrayed PDMS with Controllable Wettability Gradient by One-Step Femtosecond Laser Drilling for Ultrafast Underwater Bubble Unidirectional Self-Transport

Chao Chen, Lu-An Shi, Zhouchen Huang, Yanlei Hu, Sizhu Wu, Jiawen Li,\* Dong Wu,\* and Jiaru Chu

Achieving the unidirectional transportation of bubbles in the liquid phase is of great importance for solving both academic and industrial issues. Here, Janus (hydrophobic and superhydrophobic surfaces) microhole-arrayed polydimethylsiloxane fabricated by one-step femtosecond laser drilling for ultrafast underwater bubble unidirectional transportation is reported. In aqueous solution, bubbles selectively penetrate from an aerophilic side to a superaerophilic one in the direction of both buoyancy and antibuoyancy, but are blocked in a reverse direction. More importantly, the bubbles readily penetrate through this Janus system within 81 ms, which is two orders of magnitude shorter than that of a previous Janus one because the aerophilic surface of current Janus system is more favorable for capturing and transporting the bubble than the superaerophobic surface of Janus system. Additionally, this “diode” presents a switchable property, which is dependent on the laser exposure dosage. According to X-ray photoelectron spectroscopy spectrum, the underlying mechanism is that the excessive laser exposure dosage is inclined to induce the graft of oxyhydril group as the substitution of the original hydrocarbonyl group. This work may provide an innovatory insight for designing advanced materials for ultrafast gas bubble directional transportation/collection in aqueous media, in addition to gas/liquid separation.

## 1. Introduction

Underwater bubbles are significant fluid systems that have attracted great research interest because of their enormous potential applications in photovoltaic and environmental-remediation areas.<sup>[1–4]</sup> The presence of gas bubbles is sometimes contributive to elevating heat transfer in the ocean.<sup>[5,6]</sup> Nevertheless, the gas bubbles generated during the exploitation of crude oil including carbon dioxide, hydrogen sulfide, and oxygen can lead to the severe corrosion for the transporting pipes, which is inclined to shorten equipment lifetimes and increase resource consumption.<sup>[7,8]</sup> In consequence, realizing the controllable transportation of underwater bubbles is of great importance for solving practical issues.


Inspired by the unidirectional fluid transportation,<sup>[9–17]</sup> researchers have revealed that the dominant factor playing the decisive role in achieving

the unidirectional transportation of underwater gas bubbles should be assigned to the asymmetric wettability of a Janus system (an integration of hydrophobic and hydrophilic surface). On the basis of this strategy, great efforts have been paved to realize this target (Table 1). For the first time, Chen et al. employed a Janus copper mesh that had been decorated with a layer of hydrophilic TiO<sub>2</sub> nanoparticles on the upper face and grafted a layer of hydrophobic dodecanethiol on the lower surface to fabricate an air “diode,” which endowed the mesh with an admired underwater bubble unidirectional transportation property.<sup>[18]</sup> Besides, Yong et al. utilized a Janus hierarchical through microhole-arrayed (MHA) polydimethylsiloxane (PDMS) sheet with an intrinsic hydrophobic upper surface and a hydrophilic lower surface that had been modified by oxygen plasma to realize a selective passage for underwater bubbles.<sup>[19]</sup> Recently, Pei et al. demonstrated an antibuoyancy unidirectional transportation of bubbles by using an integrated Janus copper mesh, which had been modified by chemical etching to induce a superaerophobic upper surface and n-tetradecyl mercaptan/ethanol solution to obtain an aerophilic (AL) lower surface.

Dr. C. Chen, Dr. Z. Huang, Prof. Y. Hu, Prof. J. Li, Prof. D. Wu, Prof. J. Chu  
 CAS Key Laboratory of Mechanical Behavior and Design of Materials  
 Department of Precision Machinery and Precision Instrumentation  
 University of Science and Technology of China  
 Hefei 230026, China  
 E-mail: jwl@ustc.edu.cn; dongwu@ustc.edu.cn

Dr. L.-A. Shi  
 Division of Nanomaterials and Chemistry  
 Hefei National Laboratory for Physical Sciences at the Microscale  
 Collaborative Innovation Center of Suzhou Nano Science and Technology  
 CAS Center for Excellence in Nanoscience  
 Hefei Science Center of CAS  
 Department of Chemistry  
 University of Science and Technology of China  
 Hefei 230026, China

Prof. S. Wu  
 School of Instrument Science and Opto-Electronics Engineering  
 Hefei University of Technology  
 Hefei 230009, China

 The ORCID identification number(s) for the author(s) of this article can be found under <https://doi.org/10.1002/admi.201900297>.

DOI: 10.1002/admi.201900297

**Table 1.** Comparison of key parameters for manipulating gas bubbles in aqueous media using gas bubble “diodes.”

Architecture	Materials	Method	Bubble penetrating orientation	Penetration time [ms]	Ref.
Aerophilic/aerophobic	Copper mesh	Chemical etching	Antibuoyancy	70	[20]
Aerophilic/aerophobic	Copper mesh	TiO <sub>2</sub> NPs modification and chemical etching	Buoyancy	35 000	[18]
Aerophilic/aerophobic	Aluminum foil	Fluorination and laser drilling	Buoyancy	1720	[47]
Aerophilic/aerophobic	PDMS	Laser drilling and plasma treatment	Buoyancy	NA	[19]
Aerophilic/aerophobic	PDMS	One-step femtosecond laser drilling	Buoyancy and antibuoyancy	764	This work
Aerophilic/superaerophilic	PDMS	One-step femtosecond laser drilling	Buoyancy and antibuoyancy	81	This work

So gas bubbles readily passed through the composite mesh from the superaerophobic side but were blocked from the opposite side.<sup>[20]</sup> More recently, Waldman et al. first produced Janus porous poly(propylene) membranes consisting of a compositional gradient ranging from hydrophilic Al<sub>2</sub>O<sub>3</sub> on one face to hydrophobic poly(propylene) on the opposite face utilizing an atomic layer deposition (ALD) method.<sup>[21]</sup> Therein, the key parameter optimization for ALD system enabled the resultant Janus membrane reducing bubble size in an aeration process and improving gas delivery. In summary, the unidirectional transportation property for underwater bubbles should be attributed to a Janus architecture. However, several severe disadvantages has to be listed as: (1) Tedious chemical etching and modifying processes are both not environment-friendly and time-consuming,<sup>[18,20]</sup> (2) wettability modification using oxygen plasma is well-known unstable,<sup>[22]</sup> (3) bubble penetrated the Janus mesh with a typical period of 35 s revealing an in-efficient bubble collection efficiency,<sup>[18]</sup> (4) penetration process is dependent on the positive force arising from the injection syringe signifying an impractical application potential,<sup>[20]</sup> and (5) convenient and scalable production of Janus system without pumping vacuum is still a blockage.<sup>[21]</sup> In this regard, there is still an urgent need to explore a facile, high-efficiency, and highly reliable method to promote the practical applications of underwater bubble manipulation.

Herein, we first report an innovative Janus underwater gas bubble “diode” on the basis of MHA PDMS sheet that was manufactured via one-step femtosecond laser ablation. For clarifying, the current Janus “diode” allowed the gas bubbles penetrate from an AL surface toward a superaerophilic (SAL) surface, whereas it was blocked from the opposite direction. By carefully optimizing the morphology of these tapered microholes, a typical air bubble (40 μL) could penetrate through the Janus MHA PDMS sheet in an ultrashort period of 81 ms on account of the driving forces provided by the wettability gradient, Laplace pressure, and buoyancy. Besides, the wettability gradient orientation could be dramatically switchable by regulating the laser parameters, revealing the underwater air bubble unidirectional penetration was tunable. Moreover, the giant wettability gradient of the MHA PDMS membranes has endowed the underwater bubbles with remarkable antibuoyancy unidirectional penetration property. This work demonstrates a promising methodology for guiding the smart manipulation of bubbles in water, and extends the application of smart membranes with asymmetric wettability.

## 2. Results and Discussion

### 2.1. Facile Fabrication of MHA PDMS and Its Application in Underwater Bubble Unidirectional Self-Transportation

The Janus MHA PDMS could be readily harvested after a spin-coating, curing, and a subsequent laser drilling process. First, the liquid PDMS mixture (≈5 mL) was poured into a glass culture dish, which was then transferred to a spin-coater equipped with a vacuum pumping and allowed to rotate for 20 s at 300 rpm (Figure 1a). Thereafter, a flexible PDMS membrane with ≈210 μm thickness could be obtained after annealing at 80 °C for 1 h (Figure 1f). Due to the unique advantages of a femtosecond laser ablation technique such as noncontact manufacturing, very small heat affected zone formation around the ablated area, and high spatial resolution,<sup>[23–26]</sup> the tailored PDMS membrane was processed into an ideal tapered topography using a focusing mode. Because of a Gaussian beam essence, the upper surface and lower surface were supposed to be induced with differential morphologies (Figure 1b,d). This morphology difference endowed both sides with different roughness and wettability (Figure 1c,e). Additionally, the roughness gradients through the thickness of a typical micro-hole had also been convinced by scanning electron microscopy (SEM) insights (Figure S1, Supporting Information). In regard of atomic force microscope (AFM) as an effective technique to characterize the roughness of micro/nanostructures, the average roughness ( $R_a$ ) values assigned to the larger-pore surface (LPS) and smaller-pore surface (SPS) were calculated as 186 and 15 nm (Figure 1g,h), respectively. This resultant MHA PDMS was then carried out for the investigation of underwater bubble penetration behavior. Beyond our expectation, the underwater bubble was inclined to pass through this MHA PDMS in succession when a AL SPS with a smaller water contact angle (WCA) of  $95 \pm 3^\circ$  was put downward, whereas the bubble tended to be blocked once it was ejected from the SAL LPS with a larger WCA of  $147 \pm 5^\circ$ . As a result, this Janus system could be considered as a bubble “diode” (Figure 1i,j).

### 2.2. Morphology Regulation of MHA PDMS and Their Switchable Wettability Gradients

Femtosecond laser microfabrication is one of the most effective techniques for inducing diverse micro/nanostructures on material surfaces.<sup>[27–33]</sup> Thus, femtosecond laser microfabrication has recently been extensively applied for designing and controlling

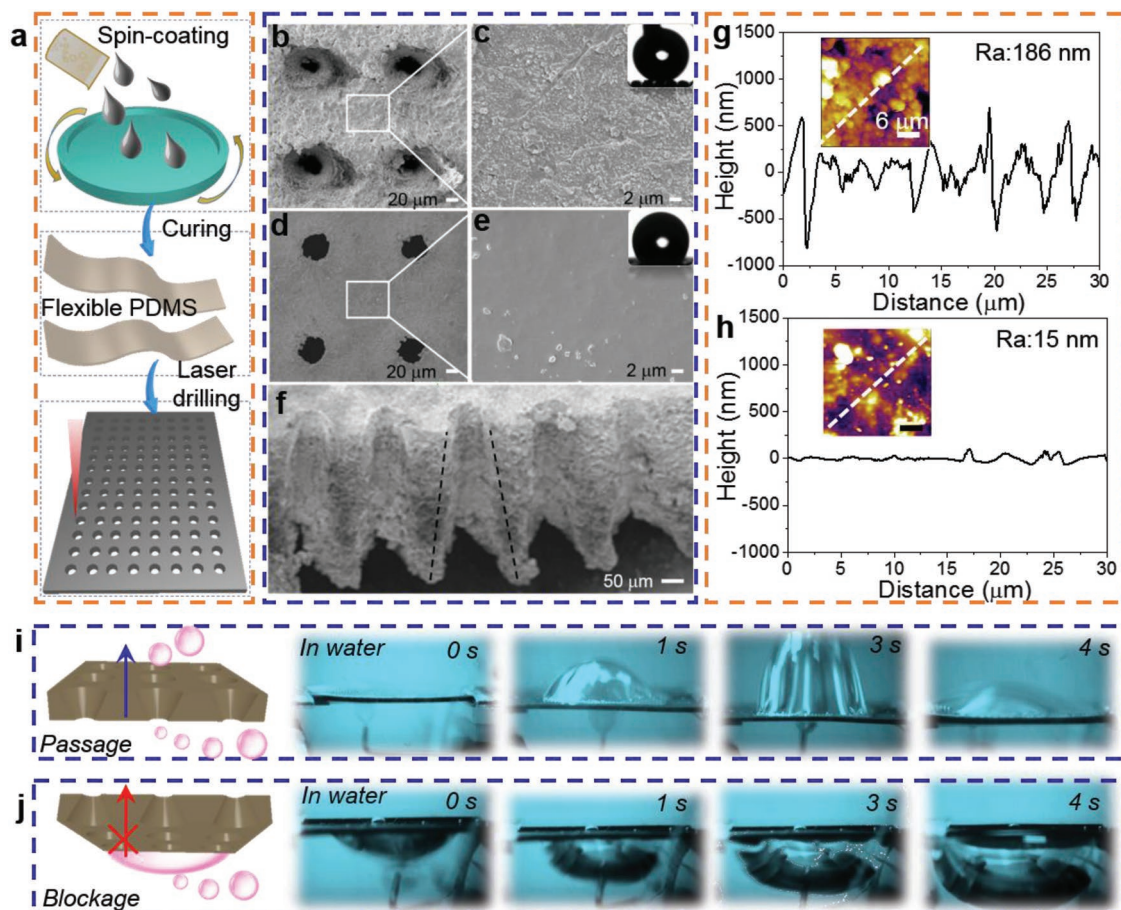


**Figure 1.** One-step fabrication of highly uniform MHA PDMS using a femtosecond laser and its applications in underwater bubble unidirectional penetration. a) Schematic diagram for preparing MHA PDMS including spin-coating, curing, and a subsequent femtosecond laser drilling process. b,d) SEM images for the larger-pore surface (LPS) and smaller-pore surface (SPS) of the resultant MHA PDMS, respectively. c,e) The enlarged SEM images for characterizing the roughness difference located on both sides in (b) and (d), respectively. The insets are digital pictures exhibiting the water wettability on both sides of this typical MHA PDMS. f) Sectional view of the manufactured MHA PDMS (tilt angle:  $80^\circ$ ). g,h) Roughness curves obtained from atomic force microscope (AFM) to verify the presence of a giant wettability gradient between LPS and SPS, respectively. i,j) Digital pictures for underwater bubbles ejected from SPS to LPS and LPS to SPS of the fabricated MHA PDMS, respectively.

the surface wettability of materials.<sup>[34–42]</sup> In this view, we successfully combined the mechanical drilling technique and femtosecond laser ablation to harvest a series of MHA PDMS samples by regulating the laser exposure dosage (Figure 2a,b). As shown in Figure 2c, the average hole diameter assigned to the LPS and SPS was characterized as 127.8/129.7/131.4/132.7/130.4 and 25.2/51.3/85.1/108.3/129.6  $\mu\text{m}$ , respectively. There was no obvious variation for the pore size of the upper surface in comparison with that of the lower surface exhibiting a linear elevation tendency. As the laser pulse number increased from 50 to 250 with an interval of 50, the WCA of lower surface increased from  $99^\circ$  to  $112^\circ$ ,  $165^\circ$ ,  $174^\circ$ , and  $150^\circ$  (Figure 2d). This is because the surface roughness enhanced as the laser exposure dosage increased, just as what we expected. However, the WCA of the upper surface first increased from  $127^\circ$  to  $159^\circ$  and  $163^\circ$ , then decreased to  $124^\circ$  and  $135^\circ$ . In sharp contrast, the underwater bubble contact angle (UBCA) is just the complementary (Figure 2e).<sup>[19]</sup>

We deduced the possible reason is the variation of the surface chemical property. Herein, typical X-ray photoelectron

spectroscopy (XPS) spectrums of sample-2 (100 pulse numbers) and sample-4 (200 pulse numbers) had been conducted for the investigation of this abnormal phenomenon (Figure S2, Supporting Information). Accordingly, peak-differentiating and imitating had been implemented for C1s, O1s, and Si2p, respectively. Therein, peaks at 102.3 and 103.5 eV for Si2p should be assigned to the binding energy of Si–OH and Si–O–Si (Figure 3a), respectively. Whereby, we could detect that the ratio of Si–OH and Si–O–Si in sample-4 exhibited a sharp increase comparing to that in sample-2, which signified that excessive laser dosage would lead to the increase of hydroxy group. In addition, O1s peak was disassembled to two separate peaks at 532.3 and 532.8 eV that were attributed to the binding energy of O–H and O–Si, where we found hydroxy group indeed increased when excessive laser dosage was applied (Figure 3b). Furthermore, the decompose peaks at 284.6 and 285.2 eV presented the binding energy of C–Si and C–H (Figure 3c), where the relative ratio of C–H and C–Si exhibited slightly decrease in sample-4. Moreover, the quantitative analysis for Si2p, O1s, and C1s was also executed by virtue of a normalization method,

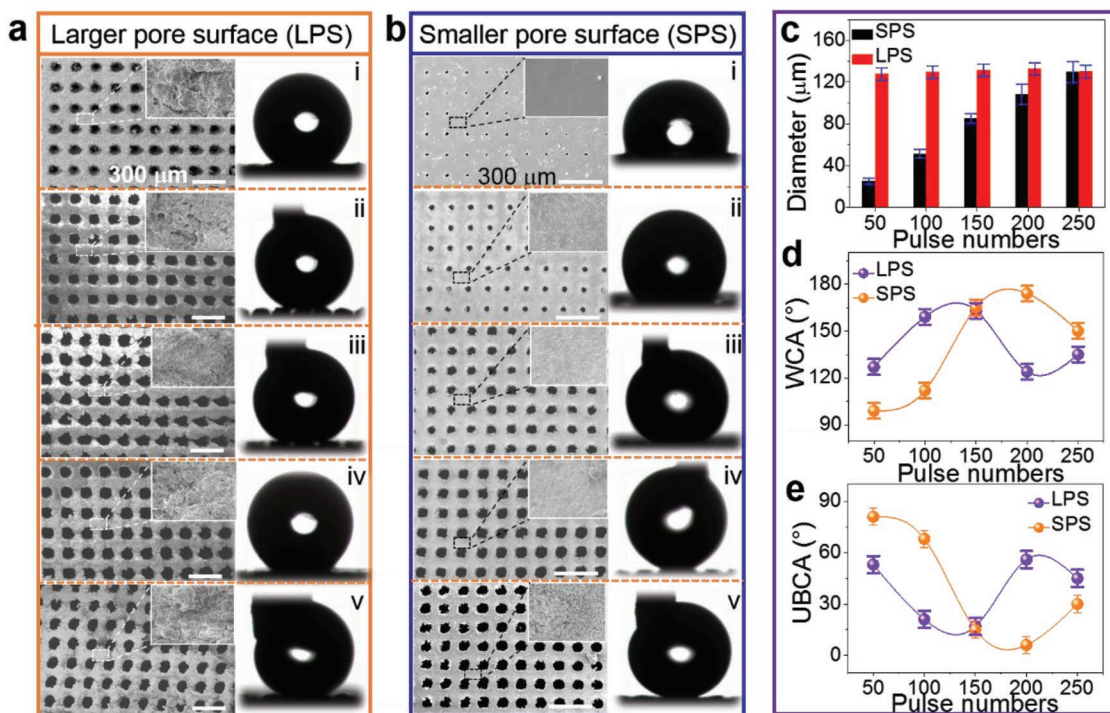


**Figure 2.** Morphology regulation of MHA PDMS by one-step femtosecond laser drilling and their characterizations. a,b) SEM images and water wettabilities for LPS and SPS of the MHA PDMS fabricated by applying the pulse numbers of 50, 100, 150, 200, and 250, respectively. The insets are the enlarged SEM images to characterize the surface roughness change. c–e) The corresponding diameter variations, measured WCAs, and theoretical UBCA values for the LPS and SPS of five samples, respectively.

we can further conclude that the excessive laser pulse number can modify the relative content of hydroxy group and a subsequent PDMS surface wettability (Table S1, Supporting Information). As a consequence, the mechanism of this switchable property should be revealed as follows: (1) When the fewer laser pulse numbers (<100) were applied, the induced micro/nanostructure dominated the surface wettability (superhydrophobic) and the molecular chains in PDMS did not suffer from destruction because of a smaller heat effect. (2) In contrast, once excessive pulse numbers (>200) had been supplied, hydrocarbonyl group would be cut off due to the colossal heat effect and then the hydroxyl group derived from the water in air was inclined to decorate on the “wound” to weaken its hydrophobic property (Figure 3c).

Accordingly, based on the Janus MHA PDMS with differential wettability gradients, underwater bubble unidirectional penetration was achieved in an aqueous environment (Movie S1, Supporting Information). Air bubbles were supplied continuously by a syringe needle located under MHA PDMS. As shown in parts (d) and (e), when the AL SPS was put downward, the tiny air bubbles primarily merged into a big bubble and maintained a hemispherical shape. Simultaneously, the lower air bubble would penetrate through the membrane and continuously transport upward, revealing the “forward direction” of this underwater air “diode.” The penetrated air bubbles spread and attached on the upper surface, until the buoyant force was enough to pull the bubble out of the membrane. The lower air bubbles can be completely transported to the upper surface driven by the wettability gradient. In contrast, when

the SAL LPS was fixed downward, the air bubbles tended to be blocked at the lower surface and spread horizontally, indicating the “reverse direction” of this air bubble “diode.” However, it is noteworthy that air bubbles could pass through this “diode” in both directions due to the absence of wettability gradient (Figure 3f). Hereafter, with the increase of the laser pulse number, air bubbles were dramatically switched to penetrate from the AL LPS to SAL SPS but presented a blockage in the reverse direction, demonstrating this “diode” direction was dominated by the wettability gradient (Figure 3g,h). In addition, no obvious variation of the wettability gradient had been observed after 300 consecutive tests (Figure S3, Supporting Information) and the bubble unidirectional penetration results do not change at least for a month, demonstrating the excellent stability of this non-Janus bubble “diode” (Figure S4, Movie S2, Supporting Information).

### 2.3. Hydrokinetic Mechanism Exploration for Underwater Bubble Unidirectional Penetration Behavior

To explore the kinetic mechanism of the underwater bubble unidirectional transportation process, high-speed camera was employed to investigate this penetration behavior. In regard of a typical Janus system (sample-2) with the experimental UBCAs of  $110 \pm 5^\circ$  (SPS) and  $24 \pm 3^\circ$  (LPS), air bubble with the volume of  $40 \mu\text{L}$  was allowed to penetrate through this Janus MHA PDMS in 764 ms when the aerophobic (AB) surface was fixed downward (Figure 4a, Movie S3, Supporting

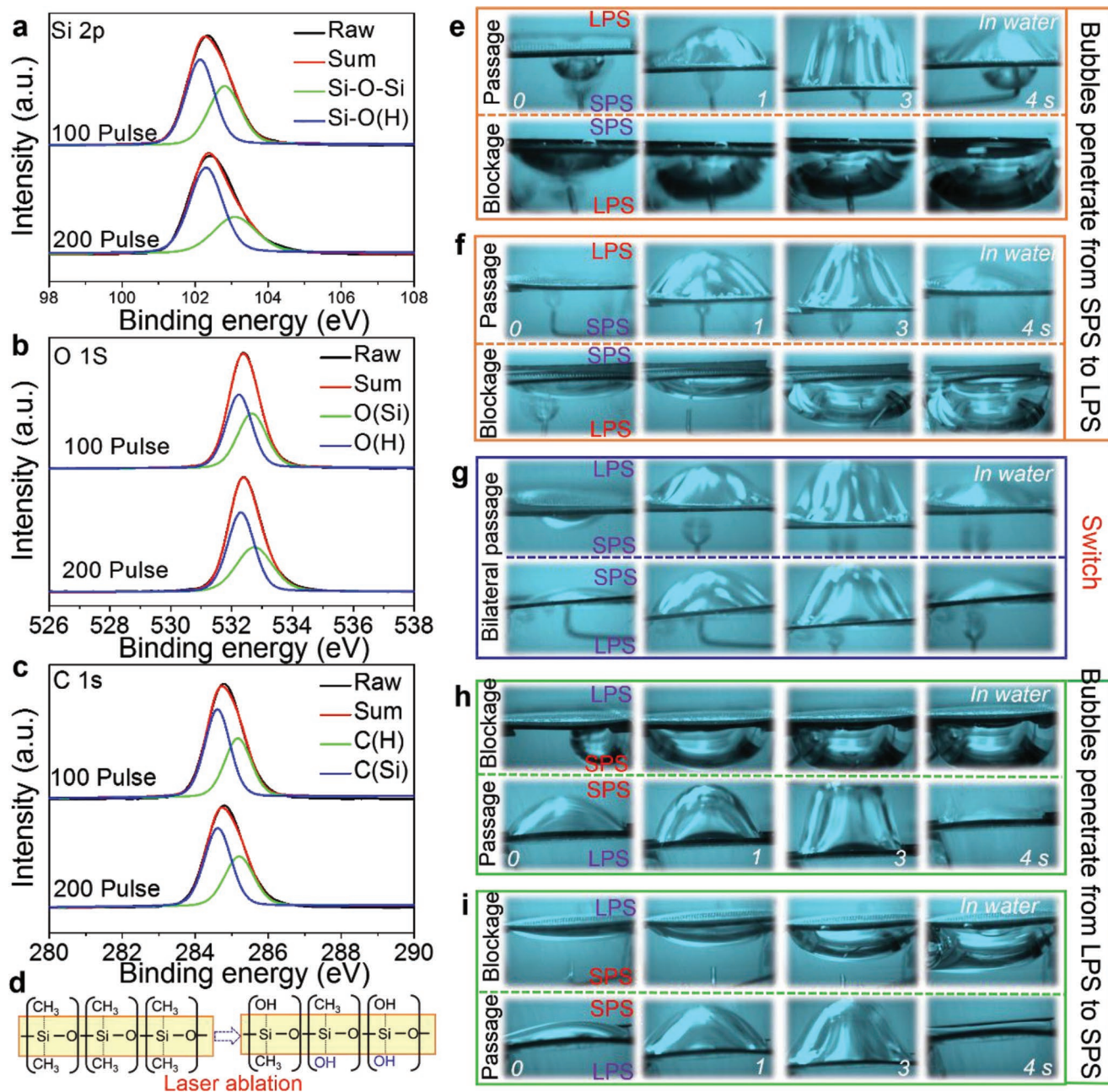


**Figure 3.** Real-time monitoring of the underwater bubble unidirectional penetration for five MHA PDMS so-called “bubble diodes” and their switchable wettability gradient orientations. a–c) XPS spectrums assigned to Si2p, O1s, and C1s in sample-2 and sample-4, respectively. d) Schematic mechanism for illustrating the variation of functional groups of MHA PDMS after suffering from the excessive laser ablation. e, f) The captured digital pictures of underwater bubble penetration/blockage for sample-1 and sample-2 when we put the SPS downward/upward. g) Extracted images of the underwater bubble penetration behavior for sample-3. h, i) Digital pictures of underwater bubble blockage/penetration for sample-4 and sample-5 when we put the SPS downward/upward.

Information). However, once the AL surface was fixed downward, the bubble would spread along the horizontal direction and present an in situ expansion behavior. In contrast, for another typical Janus system (sample-4) with the measured UBCAs of  $13 \pm 4^\circ$  (SPS) and  $30 \pm 3^\circ$  (LPS), the bubble ( $40 \mu\text{L}$ ) penetrated from the AL side to a SAL one in an ultrashort period of 81 ms (Figure 4b, Movie S4, Supporting Information).

In view of the classical fundamental physics, the underwater bubble penetration process should be subjected to four crucial forces:

- (1) Buoyancy is a contributive force to promote the bubble unidirectional penetration upward but a resistive force for the antibuoyancy penetration downward, which could be written as

$$F_b = \rho_w g V_{\text{bubble}} \quad (1)$$

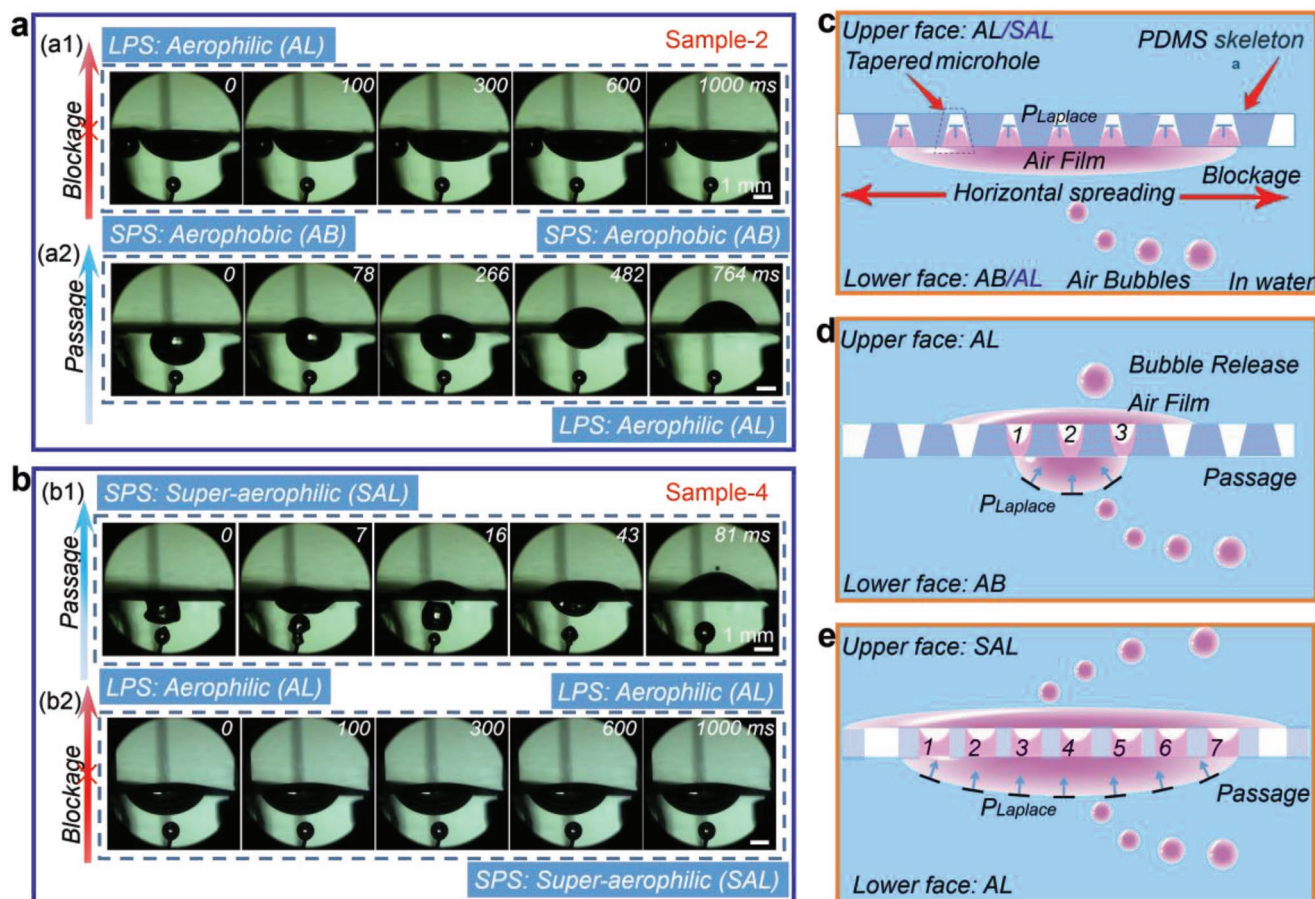


**Figure 4.** Hydrokinetic mechanism exploration for underwater bubble unidirectional penetration behavior by taking advantage of an ultrahigh speed camera. a2,b1) The captured digital pictures of an air bubble (40 μL) penetrated from an aerophobic (AB) surface to an aerophilic (AL) surface for sample-2 and from an AL surface to a superaerophilic (SAL) surface for sample-4. a1,b2) The extracted images of an air bubble (40 μL) ejected from an AL surface to AB surface for sample-2 and from a SAL surface to an AL surface for sample-4, respectively. c) Schematic diagram for the force analysis of underwater bubbles ejected from an AB surface to an AL surface or from an AL surface to a SAL surface, where the Laplace pressure applied on the bubbles is downward and inclined to stop the bubbles from penetration. d,e) Schematic diagrams for the underwater bubbles penetrating through this Janus system from an AB surface to an AL surface and from an AL surface to a SAL surface.

where  $\rho_w$ ,  $g$ , and  $V_{\text{bubble}}$  are the mass density of water, gravitational acceleration, and volume of the bubble, respectively. Here,  $\rho_w$ ,  $g$ , and  $V_{\text{bubble}}$  are known as  $1 \text{ g mL}^{-1}$ ,  $9.8 \text{ N kg}^{-1}$ , and  $40 \text{ μL}$ , respectively. Thus, the corresponding  $F_b$  was calculated as  $39.2 \times 10^{-3} \text{ N}$  in this work.

(2) Laplace pressure ( $P_{\text{Laplace}}$ ) sometimes acts as a positive driving force, but sometimes is a resistance for the underwater bubble unidirectional penetration, which can be described by the Young–Laplace equation<sup>[20]</sup>

$$P_{\text{Laplace}} = \gamma \left( \frac{1}{R_1} - \frac{1}{R_2} \right) \quad (2)$$

where  $\gamma$  is the surface tension of water ( $7.2 \times 10^{-2} \text{ N m}^{-1}$ ),  $R_1$  is the radius of curvature of the bubble, and  $R_2$  is the radius of curvature of the air gas film. Once the underwater bubbles were ejected from the AL surface to SAL surface, the resultant  $P_{\text{Laplace}}$  was inclined to stop the bubbles from penetration, where  $P_{\text{Laplace}}$  was considered as a resistance (Figure 4c). However, in a reverse direction,  $P_{\text{Laplace}}$  turned to behave as a contributor for the underwater bubble unidirectional

transportation. For both Janus MHA PDMS membranes,  $R_2$  is infinity because of an AL/SAL upper surface.  $R_{1\text{-sample-2}}$  and  $R_{1\text{-sample-4}}$  are estimated as 1.5 and 2.0 mm. Hence, the corresponding  $P_{\text{Laplace}}$  are estimated as 48 and 36 kPa, respectively. Ulteriorly,  $F_{\text{Laplace}}$  could be calculated by the following equations

$$F_{\text{Laplace}} = P_{\text{Laplace}} \times S_{\text{SV}}, \quad S_{\text{SV}} = \frac{\pi}{4} D_{\text{SV}}^2 \quad (3)$$

where  $S_{\text{SV}}$  and  $D_{\text{SV}}$  present the contact area and local diameter of the air bubble attaching to a solid-phase MHA PDMS before the bubble spontaneous penetration coming forth. Since  $D_{\text{SV-sample-2}}$  and  $D_{\text{SV-sample-4}}$  had been measured as 2.1 and 3.5 mm, the approximate values for  $F_{\text{Laplace-sample-2}}$  and  $F_{\text{Laplace-sample-4}}$  were calculated as 16.9 and 35.3 N, respectively. In consequence, the bubble penetration rate for AL/SAL system is much faster than that of AB/AL system, which should be partially attributed to a larger  $F_{\text{Laplace}}$ .

(3) Intrusion pressure as a microstructure-derived resistance displays a conclusive role in determining the underwater

bubble penetration behavior, which can be calculated by the relationship<sup>[20,43]</sup>

$$P_{\text{int}} = \frac{4\gamma|\cos\theta|}{D} \quad (4)$$

where  $\gamma$ ,  $D$ , and  $\theta$  refer to the surface tension of water, pore diameter, and UBCA of the AL surface, respectively. The larger the AL surface hole diameter is, the easier the bubbles pass through. Numerical calculations have been conducted for five disparate samples (Figure S5, Supporting Information), where we found  $P_{\text{int-sample-2}}$  is twofold larger than  $P_{\text{int-sample-4}}$ , indicating the latter is much more favorable for bubble passage because of a relative resistance.

(4) Wettability gradient force ( $F_{\text{wet-grad}}$ ) has been demonstrated as a dominant factor in affecting the bubble hydromechanics and written as<sup>[44–46]</sup>

$$F_{\text{wet-grad}} = \int_{l_{\text{bottom}}}^{l_{\text{top}}} \gamma(\cos\theta_A - \cos\theta_R) dl \quad (5)$$

In this equation, we confused both the surface roughness gradient and chemical wettability gradient. So, the equation and analysis were modified.

From Young's equation, the driving force can be given by

$$F_{\text{wet-grad}} = \gamma \times |\cos\theta_{\text{top}} - \cos\theta_{\text{bottom}}| \times l \quad (6)$$

where  $\gamma$  is the surface tension of water ( $7.2 \times 10^{-2} \text{ N m}^{-1}$ ).  $\theta_{\text{top}}$  and  $\theta_{\text{bottom}}$  refer to the UBCA of LPS and SPS of MHA PDMS, respectively.  $l$  is the thickness of MHA PDMS, which is regarded as a constant of  $\approx 210 \mu\text{m}$ . Accordingly, the corresponding  $F_{\text{wet}}$  for sample-2 and sample-4 had been obtained as  $8.4 \times 10^{-6}$  and  $6.6 \times 10^{-6} \text{ N}$  (Figure S6, Supporting Information), respectively. In regard of  $F_{\text{wet-grad}} \ll F_B < F_{\text{Laplace}}$ , we deduce that wettability gradient is only determining the orientation of Laplace force. So, the underwater bubbles spontaneous unidirectional self-transportation was dominated by the wettability gradient orientation.

In conclusion, the velocity of underwater bubble penetrated through AL/SAL MHA PDMS is much faster than that of a AB/AL one for one order of magnitude, which should be attributed to the following two reasons. First, the wettability gradient for the former was initiated by an AL surface and a SAL surface in comparison with the latter integrated by an AB surface and an AL surface. The former with more extensive contact area and larger  $F_{\text{Laplace}}$  had endowed the underwater bubble with more penetration channels and bigger impetus in comparison with the latter (Figure 4d,e). Second, from the view of intrusion pressure, the pore diameter for the former is  $\approx 2.5$ -fold compared with that of the latter, indicating the former with a smaller  $P_{\text{int}}$  endowed the underwater bubbles with the less resistance to penetrate through.

#### 2.4. Underwater Bubble Antibuoyancy Unidirectional Penetration

We now explore underwater bubble unidirectional penetration in circumstances where the gas bubbles penetrated against the buoyancy in water. In order to get rid of the influence of the Laplace force originating from the injection syringe, we ejected the bubbles along the horizontal direction and enabled the bubbles to come into contact with the upper face in an unstressed situation. When a SAL surface was put upward, gas bubbles were subjected to a positive force of Laplace force ( $F_{\text{Lap-1}}$ ) and two reversely resistive forces of buoyancy ( $F_B$ ) and Laplace force derived from the wettability gradient ( $F_{\text{Lap-2}}$ ) (Figure 5a). In regard of Laplace force is inversely proportional to bubble diameter,  $F_{\text{Lap-2}}$  is far more than the sum of  $F_B$  and  $F_{\text{Lap-1}}$ . So, gas bubbles should be blocked from antibuoyancy penetration when it is ejected from SAL surface to AL one. In comparison, from the view of force analysis, antibuoyancy penetration could be achieved for gas bubbles if the AL surface was fixed upward (Figure 5b). Accordingly, a series of experimental verification had been carried out for demonstrating that current Janus MHA

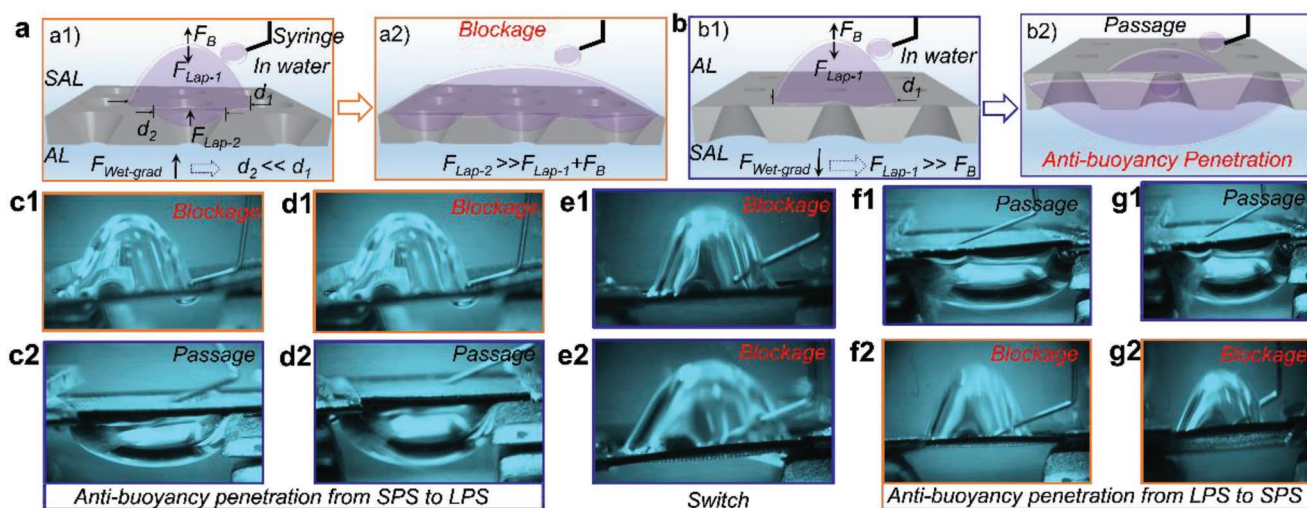


**Figure 5.** Underwater bubble antibuoyancy unidirectional self-transportation. a,b) Force analysis for gas bubbles ejected from a SAL surface to an AL one and from an AL side to a SAL one. Bubbles were ejected from the c1–g1) LPS to SPS and c2–g2) SPS to LPS for five MHA PDMS membranes, respectively.

PDMS membranes were capable of realizing antibuoyancy self-transport of underwater gas bubbles. In case of bubble ejected from the SAL side to an AL side, it was blocked on account of the resistance from the buoyancy and the upward wettability gradient induced Laplace force, whereas it would readily pass through these MHA PDMS membranes in the reverse direction because of the giant downward wettability gradient derived Laplace force overwhelming the resistance of buoyancy (Figure 5c,d). However, in the absence of the wettability gradient, the bubbles tended to exhibit the bidirectional blockage (Figure 5e). Furthermore, with the increase of the laser pulse number, the wettability gradient was switched to an inverse situation (Figure 5f,g, Movie S5, Supporting Information).

### 3. Conclusions

In this paper, a novel Janus MHA PDMS was fabricated by one-step femtosecond laser drilling. The resultant aerophilic/superaerophilic binary Janus membrane was able to realize an underwater bubble unidirectional self-transportation in the direction of both buoyancy and antibuoyancy, indicating a versatile underwater air bubble “diode.” In addition, the wettability gradient has demonstrated the decisive role in determining the underwater bubble unidirectional penetration, which is controllable by regulating the laser pulse number. Its mechanism explored by XPS spectrum is the excessive laser exposure dosage leads to the disintegration of hydrocarbyl group in PDMS and the subsequent graft of an exotic oxyhydril group. Furthermore, the numerical analysis had demonstrated this aerophilic/superaerophilic system with larger  $P_{Lap}$  and smaller  $P_{int}$  was revealed as the cooperative contributor for the underwater bubble penetration in an ultrashort period of 81 ms, which is much shorter than that of a Janus system in the previous work. The current fabrication process of the Janus system is more facile, time-saving, and efficient, which is expected to provide a new insight for the design of advanced materials for applications in ultrafast bubble capture, transportation, collection, and gas/liquid separation.

### 4. Experimental Section

**Materials:** Silicone elastomer and curing agent (Dow Corning Sylgard 170) were supplied by Suzhou Haidisi Electronics Co. Ltd. PDMS membranes were obtained by spin-coating the well-stirred mixture of A and B (5 mL) on a silicone wafer at a speed of 300 rpm and then annealed at 80 °C for 1 h. Distilled water ( $H_2O$ , 1 g  $cm^{-3}$  density) served as contact angle test materials. The underwater bubble unidirectional penetration experiments were carried out by using a NPT (normal pressure and temperature) air (20 °C, 1 atm, 1.205 × 10<sup>-3</sup> g  $cm^{-3}$  density).

**Femtosecond Laser Fabrication:** The ultrauniform tapered-microhole-array PDMS membranes were manufactured by using a mechanical drilling mode and laser ablation method. The laser beam (104 fs, 1 kHz, 800 nm) from a regenerative amplified Ti:sapphire femtosecond laser system (Legend Elite-1K-HE, Coherent, USA) was employed for ablation. During the fabrication process, the laser beam was guided onto the sample via a galvanometric scanning system (SCANLAB, Germany), which made the laser beam focus and scan along the x/y coordinate direction. The laser power, scan spacing, and speed were set at 350 mW, 200 μm, and 1 mm s<sup>-1</sup>, respectively. The MHA PDMS membranes with different lower pore size were obtained by regulating the laser pulse numbers as 100, 200, 300, 400, and 500, respectively.

**Characterization:** The micro/nanostructure induced by the laser was characterized by using a field-emission scanning electron microscope (JSM-6700F, Japan). The contact angles of the water droplet (≈4 μL) in air were measured using a CA100C contact angle system (Innuo, China) with the sessile drop method. The average values were obtained by measuring five drops at different locations on the same surface. All the contact angle measurements were conducted at 10% humidity and 20 °C temperature. The underwater bubble (40 μL) dynamic behavior on the MHA PDMS membranes was recorded using a high-speed camera (Photron-SA3) equipped with a long-distance microscope tube with a 2× magnification objective (Mitutoyo). The high-speed videos were taken using a typical rate of 5000 or 6400 frames per second (fps) and shutter speed of 1/200 000 s.

**Underwater Bubble Unidirectional Penetration Test:** Deionized (DI) water (40 mL) was added into a home-made transparent acrylic box (60 mL) equipped with two shelves to support the objective MHA PDMS membranes. The bubbles (500 μL) in water were carefully extruded using an injection syringe and adhered to an objective MHA PDMS membrane dependent on the buoyancy. Photos were taken continuously using a computer-controlled charge-coupled device (CCD) camera to show the real-time images of the bubbles on MHA PDMS membranes.

### Supporting Information

Supporting Information is available from the Wiley Online Library or from the author.

### Acknowledgements

This work was supported by the National Key R&D Program of China (2017YFB1104303, 2018YFB1105400), Fundamental Research Funds for the Central Universities (No. WK2090090024), the National Natural Science Foundation of China (Nos. 51805508, 51875544, 61805230, 51605463, and 51675503), the China Postdoctoral Science Foundation (No. 2018M642534), and Chinese Academy of Sciences Instrument Project (YZ201566). The authors acknowledge the Experimental Center of Engineering and Material Sciences at USTC for the fabrication and measuring of samples. This work was partly carried out at the USTC Center for Micro and Nanoscale Research and Fabrication.

### Conflict of Interest

The authors declare no conflict of interest.

### Keywords

air diode, antibuoyancy unidirectional penetration, femtosecond laser, Janus membranes, wettability gradient

Received: February 15, 2019

Revised: March 28, 2019

Published online:

- [1] M. Notarianni, C. A. Vernon, M. Aljada, J. Liu, N. Motta, *Sol. Energy* **2014**, *106*, 23.
- [2] A. Polman, *ACS Nano* **2013**, *7*, 15.
- [3] C. Zhang, M. Cao, H. Ma, C. Yu, K. Li, C. Yu, L. Jiang, *Adv. Funct. Mater.* **2017**, *27*, 1702020.
- [4] U. Von Gunten, *Water Res.* **2003**, *37*, 1443.



- [5] A. V. Soloviev, P. Schlüssel, *J. Phys. Oceanogr.* **1994**, *24*, 1339.
- [6] J. Gylys, T. Zdankus, M. Gylys, *Int. J. Heat Mass Transfer* **2014**, *69*, 230.
- [7] M. B. Kermani, A. Morshed, *Corrosion* **2003**, *59*, 659.
- [8] A. Samimi, *Int. J. Sci. Eng. Invent.* **2012**, *1*, 32.
- [9] J. Wang, Y. Zheng, F. Q. Nie, J. Zhai, L. Jiang, *Langmuir* **2009**, *25*, 14129.
- [10] A. R. Parker, C. R. Lawrence, *Nature* **2014**, *14*, 33.
- [11] L. Zhai, M. C. Berg, F. Ç. Cebeci, Y. Kim, J. M. Milwid, M. F. Rubner, R. E. Cohen, *Nano Lett.* **2006**, *6*, 1213.
- [12] J. Ju, H. Bai, Y. Zheng, T. Zhao, R. Fang, L. Jiang, *Nat. Commun.* **2012**, *3*, 1247.
- [13] H. Wang, J. Ding, L. Dai, X. Wang, T. Lin, *J. Mater. Chem.* **2010**, *20*, 7938.
- [14] Y. Zhao, H. Wang, H. Zhou, T. Lin, *Small* **2017**, *13*, 1601070.
- [15] J. Wu, N. Wang, L. Wang, H. Dong, Y. Zhao, L. Jiang, *Soft Matter* **2012**, *8*, 5996.
- [16] X. Tian, H. Jin, J. Sainio, R. H. Ras, O. Ikkala, *Adv. Funct. Mater.* **2014**, *24*, 6023.
- [17] H. Li, M. Cao, X. Ma, Y. Zhang, X. Jin, K. Liu, L. Jiang, *Adv. Mater. Interfaces* **2016**, *3*, 1600276.
- [18] J. Chen, Y. Liu, D. Guo, M. Cao, L. Jiang, *Chem. Commun.* **2015**, *51*, 11872.
- [19] J. Yong, F. Chen, J. Huo, Y. Fang, Q. Yang, J. Zhang, X. Hou, *Nanoscale* **2018**, *10*, 3688.
- [20] C. Pei, Y. Peng, Y. Zhang, D. Tian, K. Liu, L. Jiang, *ACS Nano* **2018**, *12*, 5489.
- [21] R. Z. Waldman, H. C. Yang, D. J. Mandia, P. F. Nealey, J. W. Elam, S. B. Darling, *Adv. Mater. Interfaces* **2018**, *5*, 1800658.
- [22] B. Da Silva, M. Zhang, G. Schelcher, L. Winter, C. Guyon, P. Tabeling, D. Bonn, M. Tatoulian, *Plasma Processes Polym.* **2017**, *14*, 1600034.
- [23] A. Y. Vorobyev, C. Guo, *Laser Photonics Rev.* **2013**, *7*, 385.
- [24] K. Sugioka, Y. Cheng, *Appl. Phys. Rev.* **2014**, *1*, 041303.
- [25] K. Sugioka, Y. Cheng, *Light: Sci. Appl.* **2014**, *3*, e149.
- [26] T. C. Chong, M. H. Hong, L. P. Shi, *Laser Photonics Rev.* **2010**, *4*, 123.
- [27] J. Yong, F. Chen, Q. Yang, X. Hou, *Soft Matter* **2015**, *11*, 8897.
- [28] D. Wu, Q. D. Chen, L. G. Niu, J. N. Wang, J. Wang, R. Wang, X. Hong, H. B. Sun, *Lab Chip* **2009**, *9*, 2391.
- [29] Z. Deng, F. Chen, Q. Yang, H. Bian, G. Du, J. Yong, S. Chao, X. Hou, *Adv. Funct. Mater.* **2016**, *26*, 1995.
- [30] C. Shan, F. Chen, Q. Yang, Y. Li, H. Bian, J. Yong, X. Hou, *Opt. Lett.* **2015**, *40*, 4050.
- [31] K. Yin, S. Yang, X. Dong, D. Chu, J. Duan, J. He, *Appl. Phys. Lett.* **2018**, *112*, 243701.
- [32] J. Duan, X. Dong, K. Yin, S. Yang, D. Chu, *Appl. Phys. Lett.* **2018**, *113*, 203704.
- [33] K. Yin, S. Yang, X. Dong, D. Chu, X. Gong, J. Duan, *Appl. Surf. Sci.* **2019**, *471*, 999.
- [34] F. Chen, D. Zhang, Q. Yang, J. Yong, G. Du, J. Si, F. Yun, X. Hou, *ACS Appl. Mater. Interfaces* **2013**, *5*, 6777.
- [35] D. Zhang, F. Chen, Q. Yang, J. Yong, H. Bian, Y. Ou, J. Si, X. Meng, X. Hou, *ACS Appl. Mater. Interfaces* **2012**, *4*, 4905.
- [36] J. Yong, F. Chen, Q. Yang, D. Zhang, U. Farooq, G. Du, X. Hou, *J. Mater. Chem. A* **2014**, *2*, 8790.
- [37] J. Yong, F. Chen, Q. Yang, Y. Fang, J. Huo, X. Hou, *Chem. Commun.* **2015**, *51*, 9813.
- [38] J. Yong, Y. Fang, F. Chen, J. Huo, Q. Yang, H. Bian, G. Du, X. Hou, *Appl. Surf. Sci.* **2016**, *389*, 1148.
- [39] J. Yong, F. Chen, Q. Yang, Y. Fang, J. Huo, J. Zhang, X. Hou, *Adv. Mater. Interfaces* **2017**, *4*, 1700552.
- [40] G. Li, H. Fan, F. Ren, C. Zhou, Z. Zhang, B. Xu, S. Wu, Y. Hu, W. Zhu, J. Li, Y. Zeng, X. Li, J. Chu, D. Wu, *J. Mater. Chem. A* **2016**, *4*, 18832.
- [41] K. Yin, D. Chu, X. Dong, C. Wang, J. Duan, J. He, *Nanoscale* **2017**, *9*, 14229.
- [42] S. Yang, K. Yin, D. Chu, J. He, J. Duan, *Appl. Phys. Lett.* **2018**, *113*, 203701.
- [43] B. Lefevre, A. Saugey, J. L. Barrat, L. Bocquet, E. Charlaix, P. F. Gobin, G. Vigier, *J. Chem. Phys.* **2004**, *120*, 4927.
- [44] H. Zhu, Z. Guo, W. Liu, *Chem. Commun.* **2016**, *52*, 3863.
- [45] M. K. Chaudhury, G. M. Whitesides, *Science* **1992**, *256*, 1539.
- [46] S. Daniel, M. K. Chaudhury, J. C. Chen, *Science* **2001**, *291*, 633.
- [47] S. Yan, F. Ren, C. Li, Y. Jiao, C. Wang, S. Wu, S. Wei, Y. Hu, J. Li, Y. Xiao, Y. Su, D. Wu, *Appl. Phys. Lett.* **2018**, *113*, 261602.